Matter

CellPress

Article

In situ Wear Study Reveals Role of Microstructure on Self-Sharpening Mechanism in Sea Urchin Teeth

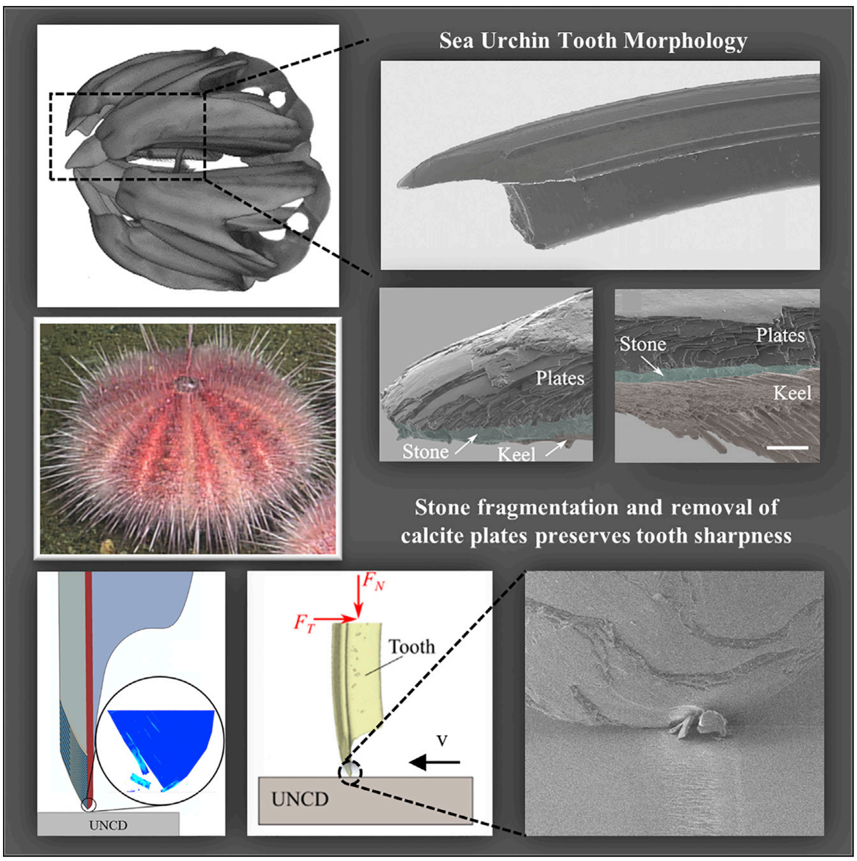

The self-sharpening of the sea urchin tooth was previously hypothesized but never visualized. Through a novel *in situ* SEM experiment, such visualization in three dimensions become possible. Moreover, when *in situ* experimental measurements were combined with nonlinear finite-element analysis, the synergy between tooth microstructural features and mechanical properties of constituents responsible for the observed self-sharpening mechanism was ascertained. Such insight of material architecture and properties is readily transferable to composite material design.

3 Understanding
Dependency and conditional studies on material behavior

Horacio D. Espinosa, Alireza Zaheri, Hoang Nguyen, David Restrepo, Matthew Daly, Michael Frank, Joanna McKittrick

espinosa@northwestern.edu

HIGHLIGHTS

Wear mechanisms of animal teeth revealed by *in situ* SEM experiments

Synergies between tooth architecture and properties of constituents ascertained

Nanomechanical experiments establish key properties of constituents and interfaces

State-of-the-art material and structural models capture visualized wear mechanisms

Espinosa et al., Matter *1*, 1246–1261
November 6, 2019
https://doi.org/10.1016/j.matt.2019.08.015

Matter

CellPress

Article

In situ Wear Study Reveals Role of Microstructure on Self-Sharpening Mechanism in Sea Urchin Teeth

Horacio D. Espinosa,[1,2,6,*] Alireza Zaheri,[1] Hoang Nguyen,[1] David Restrepo,[2,4] Matthew Daly,[2,5] Michael Frank,[3] and Joanna McKittrick[3]

SUMMARY

Animals' teeth have evolved to provide food procurement, mastication, and protection. These functions, directly linked to survival of many living animal species, require superior hardness and abrasion resistance in the animal's dentition system. Such resistance typically emerges from damage tolerance and sharpness preservation during the organism's life span. An example is the sea urchin tooth, which through gradients in mechanical properties together with exploitation of microstructural features achieves such functionality. Using contact mechanics, dimensional analysis, and a novel *in situ* scanning electron microscopy experimental methodology, conditions for tooth deformation and wear, via a self-sharpening mechanism consisting in plate chipping, were imaged and quantified. Nonlinear finite-element modeling of the self-sharpening mechanism provided insight into the synergy between constituent material properties and tooth microstructural elements. The findings reported here should inspire the design of novel tools used in machining operations, e.g., cutting and grinding, as well as in mining and tunnel boring.

INTRODUCTION

Natural materials are responsible for performing a diverse set of biological tasks to maintain the healthy condition of an organism. To meet this challenge, Nature has developed efficient strategies for the synthesis of multifunctional materials from a surprisingly limited set of constituents. In this context, it is well documented that the animal kingdom provides numerous examples of biological processes that place demanding performance requirements on natural materials systems. For example, mastication in animals requires hard and durable teeth that are capable of mechanically grinding and crushing nourishment for digestion.[1,2] For this process, animal teeth generally exhibit a hardness approaching that of metal composites and a fracture toughness comparable with those found in polymeric materials.[3,4] Furthermore, the tooth structure and constituents have evolved to withstand degradation and wearing over millions of mastication cycles throughout the lifetime of the animal.[5]

Nature provides different evolutionary strategies for maintaining the integrity of teeth. Common strategies involve the use of hard and tough outer layers on more compliant substrates, e.g., in humans and other mammals.[6–10] Others utilize replenishment, whereby the worn grinding features are renewed through continuous growth of the entire tooth structure (as in marine species such as sea urchins and chitons[11,12]). In the latter case, maintenance of sharp grinding features is of primary concern for daily feeding activities. In sea urchins, this process is hypothesized to

Progress and Potential

The teeth of animals play a crucial role in their survival, and, like other body parts, they adapted to the host's habitat to maximize their functionality. Superior performance in the sea urchin dentition system was hypothesized to emerge from sharpness preservation during the organism's life span. In this work, a novel *in situ* scanning electron microscopy experimental methodology was employed to visualize a mechanism for sharpness preservation and to quantify conditions for its activation. Nonlinear finite-element modeling, incorporating experimentally measured nanoscale properties of constituents and interfaces, provided insight into synergistic effects between tooth architecture and material properties leading to sharpness preservation. The reported findings have the potential to influence the design of tools for mining, boring, and machining operations, e.g., cutting and grinding.

be directed by a self-sharpening mechanism, whereby mineralized plates are sequentially fractured and discarded to maintain a sharp distal grinding surface.[13,14] However, it is unclear how the organism achieves a selective cleavage of tooth features from apparently brittle ceramic constituents. Conventional knowledge in the fracture behavior of ceramic materials would suggest unstable and undirected crack growth within the tooth, precluding a directed self-sharpening mechanism. The current investigation therefore seeks to reveal the relationship between sea urchin tooth architecture and constituent properties leading to tooth sharpness preservation. Moreover, the work reported here should guide the design of microstructure and selection of material constituents in the design of tools for cutting, grinding, and boring applications.

RESULTS AND DISCUSSION

Tooth Architecture

In an effort to understand the tooth-wearing mechanism, the current study examines the tribological and wear behavior of the pink sea urchin (*Strongylocentrotus fragilis*) teeth (Figures 1A–1C). Pink sea urchins are deep-sea marine species (found in a 100-m to 1-km ocean depth) that can grow up to a 10 cm in diameter.[15] Similar to other urchins, they possess hard and mineralized endo- and exoskeletons. They gain their mineral components from seawater; and have been studied for insight into the mechanisms of biomineralization.[16] Among their skeletal elements, teeth are heavily mineralized (~99% mineralized) with magnesium-enriched calcite.[17] They utilize their teeth to forage food from coral reefs, and scrape and bore holes into rocky substrates to hide from predators or to use as shelters against wave action.[18] This requires their teeth to be tough and wear resistant in abrasive (i.e., sandy) environments.

The feeding apparatus of sea urchins, commonly referred to as Aristotle's lantern, is shown in Figure 1C. This skeleton muscular system holds five teeth firmly in place, in which each jaw contains a single tooth.[19] These jaws work together as a mechanical grasping in such a way that the outward protrusion and inward withdrawal of teeth occur centripetally and simultaneously.[20] A microcomputed tomography (μ-CT) image of a segment of the whole tooth is shown in Figure 1D. The image reveals that the tooth is formed along an elliptical curve with a T-shaped cross-section. Images of transversal and longitudinal cross-sections of the tooth, displayed in Figures 1E and 1F, expose other imporant features of the tooth structure. The transversal section shows that the tooth is composed of three structural regions: the primary plates, the stone region, and the secondary plates (Figure 1E). The stone region is made of high-aspect-ratio, small-diameter fibers (micrometers in size) surrounded by an organic sheath. The fibers are embedded in a polycrystalline matrix consisting of nanometer-sized particles (10–20 nm in diameter)[21] of magnesium-rich calcite. It was reported that the level of magnesium content varies along the tooth length and is higher at the tip region, which leads to higher hardness and abrasion resistance.[22] The fiber diameter gradually increases from the stone (~1 μm) to the keel (~20 μm), where the cleavage fracture of large calcite fibers is dominant (see Figure S1). The longitudinal cross-sectional image (Figure 1F) of the stone reveals fiber fracture as well as pullout, which is due to the debonding at the interface between the fibers and the organic sheath. Primary plates are typically made of calcite single crystals and are located on the convex surface of the tooth, while the secondary plates populate the concave surface bounding the stone region laterally. The longitudinal section, shown in Figure 1G, reveals the array of curved primary plates, stacked parallel to each other. The image also shows the fibers and polycrystalline matrix filling the space between plates. The keel (Figure 1H) forms the base of the

[1]Theoretical and Applied Mechanics Program, Northwestern University, Evanston, IL, USA

[2]Mechanical Engineering, Northwestern University, Evanston, IL, USA

[3]Mechanical Engineering, University of California, San Diego, La Jolla, CA, USA

[4]Present address: Mechanical Engineering, University of Texas, San Antonio, San Antonio, TX, USA

[5]Present address: Civil and Materials Engineering, University of Illinois at Chicago, Chicago, IL, USA

[6]Lead Contact

*Correspondence: espinosa@northwestern.edu

https://doi.org/10.1016/j.matt.2019.08.015

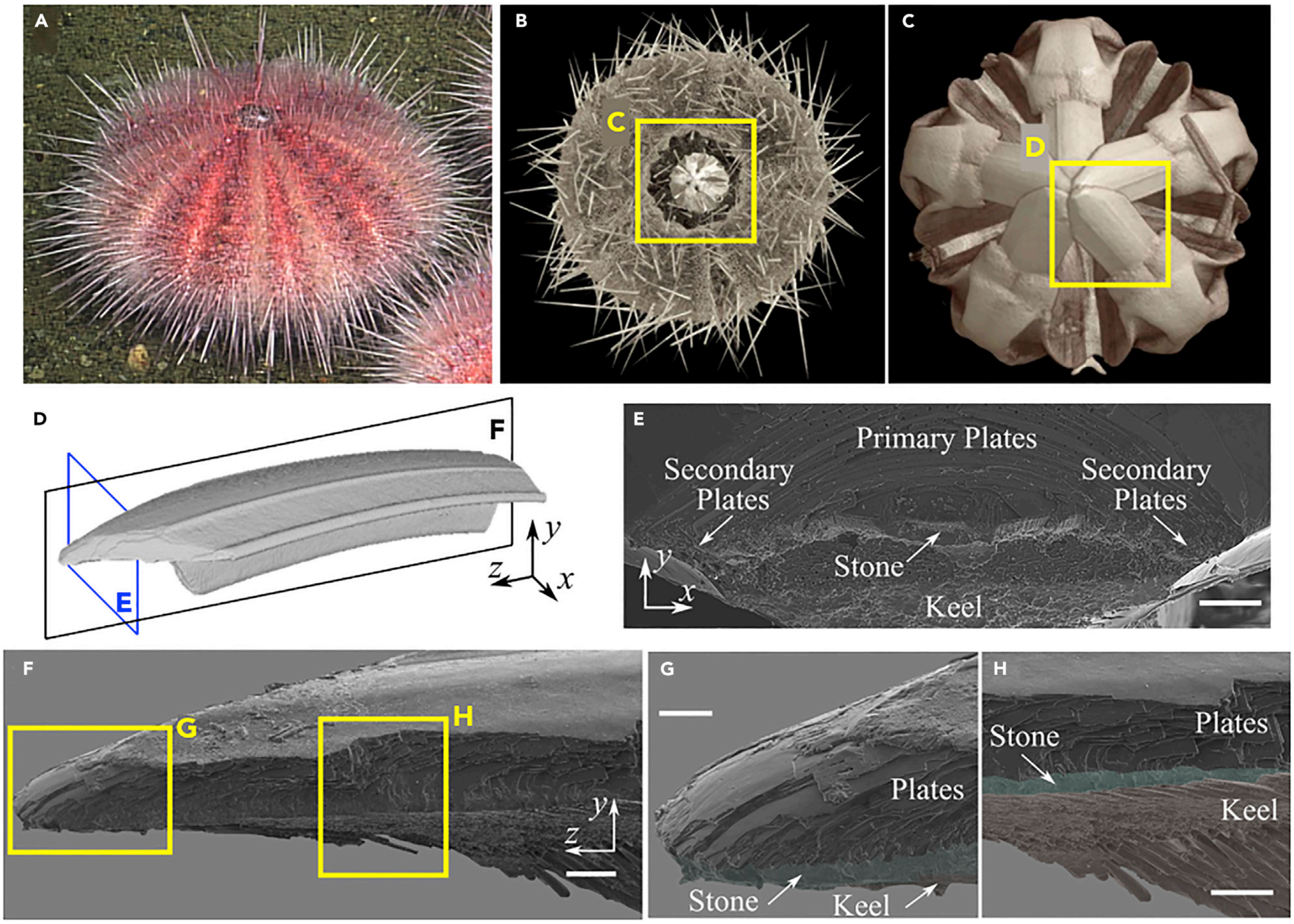

Figure 1. Overview of Sea Urchin Teeth Microstructure

(A) Pink sea urchin (*Strongylocentrotus fragilis*).

(B) Internal jaw apparatus (Aristotle's lantern).

(C) Five tooth tips stacked atop one another within the jaws.

(D) A microcomputed tomography image showing a segment of the tooth.

(E) A fractured tip of the tooth, transversal section, showing different regions: primary plates, secondary plates, stone, and keel. Scale bar, 50 μm.

(F) A longitudinal section of the fractured tooth. Scale bar, 100 μm.

(G and H) Different regions of the tooth showing the primary plates, stone, and the keel part at the tip (G) and away from the tip region (H). Scale bars, 50 μm.

T cross-section and increases the bending stiffness of the tooth. More images of the microstructure of the tooth are provided in Figure S1.

Mechanical Properties of the Tooth Constituents

To gain insight into the tooth wear mechanism, knowledge of the mechanical properties of the tooth constituents is crucial. Hence, nanoindentation and *in situ* scanning electron microscopy (SEM) micropillar compression tests were performed for this purpose. Samples sectioned along the longitudinal and transversal orientations were prepared for nanomechanical testing as described in Experimental Procedures. Low-depth indentation maps were obtained through single loading-unloading cycles with a spacing of 10 μm between each indentation. Data analysis revealed an average Young's modulus (E) and hardness (H), at the tip of the tooth in the longitudinal and transversal directions, to be $E_L = 77.3 \pm 4.8$ GPa, $H_L = 4.3 \pm 0.5$ GPa and $E_T = 70.2 \pm 7.2$ GPa, $H_T = 3.8 \pm 0.6$ GPa, respectively (Figure S2). These results are consistent with previous studies of indentation on sea urchin teeth.[21,23] In addition, indentations with cyclic incremental loading

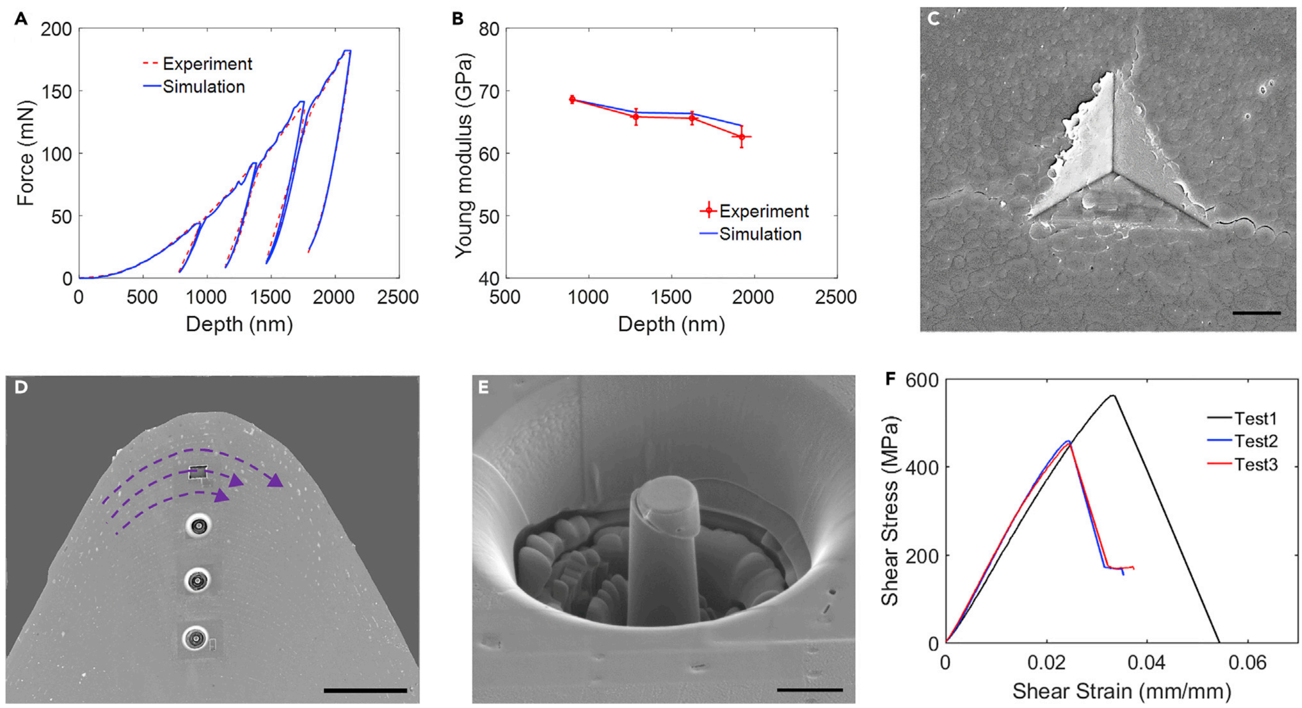

Figure 2. Probing the Nano- and Micromechanical Properties of the Tooth Tip

(A–C) Representative cyclic indentation load-displacement curve, in the stone region along the longitudinal direction (A): experimental measurement (red dashed line) and finite-element modeling simulation (blue solid line). (B) Young's modulus as a function of indentation depth: experimental measurement (red solid line) and simulated results (blue solid line). Experimental error bars correspond to one standard deviation. (C) Image of residual indentation mark at the end of the cyclic indentation. Scale bar, 5 μm.

(D) A planar section exposing interfaces (purple arrows) between calcite plates. This section is parallel to the out of-plane (x) direction, where interfaces are nominally oriented at ~30° to the x direction. Scale bar, 100 μm.

(E) Micropillar sample with failed interface. Scale bar, 5 μm.

(F) Shear stress-strain curve from micropillar compression test.

were performed in the longitudinal direction to establish a visco-plastic-damage model for the stone region. A representative indentation load-displacement curve is displayed in Figure 2A. The modulus for each cycle was calculated based on the Oliver-Pharr method[24] using the unloading data. Indentation cycles revealed a monotonic decrease in modulus with increasing indentation depth (Figure 2B). This stiffness degradation is attributed to damage accumulation through irreversible deformation, and is modeled via finite-element simulations using a visco-plastic-damage model previously employed in the modeling of bone.[25,26] Note S3 summarizes the employed constitutive law together with the procedure used for its parametrization. Experimental evidence of damage is shown in Figure 2C, where cracks are observed emanating from the corners of the indentation mark. Crack growth occurs around the fibers rather than through the fibers. This manner of crack deflection was previously observed in the fracture surface of sea urchin teeth as a result of the weak organic sheath/matrix interfaces.[27]

The mechanical properties of the tooth constituents were also assessed using micropillar quasi-static compression experiments. The micropillar tests provided information on the nature of the compressive uniaxial stress-strain behavior of the stone, as well as the strength of the interface between calcite plates. We note that micropillar compression tests were previously employed in the testing of other biomaterials such as lamellar bone.[28] Focused ion beam (FIB) milling was used to fabricate micrometer-sized pillars from the plate and the stone regions in the sea urchin tooth (see

Experimental Procedures). To assess the cohesive strength of interfaces between primary plates, in the convex side of the tooth, we fabricated micropillars at an oblique orientation relative to the normal interface. A representative set of fabricated micropillars, within the plate region, is shown in Figure 2D. There are multiple interfaces at oblique angles to the pillar axis, which enables interface characterization under shear loading when the micropillar is axially compressed (see Figure S3). A micrograph of a typical micropillar containing an oblique interface is shown in Figure 2E, where the sliding of the interface is clearly observed. The corresponding shear stress-strain curve is shown in Figure 2F, from which the interface strength can be inferred. A summary of measured mechanical properties is given in Tables S1–S4. Such properties are employed in the design of the wear tests and the parametrization of constitutive laws used in the finite-element simulations subsequently discussed.

Stress-strain curves obtained from micropillars fabricated within the stone region, along the longitudinal direction, are shown in Figure S4. Surprisingly, the measured elastic modulus is almost half the one measured via indentation testing. Such a discrepancy between indentation and micropillar compression tests was also reported for dental enamel.[29,30] Even though several explanations were advanced in the literature, from artifacts in sample preparation, e.g., ion irradiation, to environmental conditions such as humidity, the investigators could not justify the difference in the reported values. In this work, we found a size effect whereby the doubling of the size of the pillar resulted in a $\sim$30% increase in Young's modulus. We hypothesize that further increase in the micropillar size would minimize the difference in modulus measured with the two techniques. Unfortunately, the physical size of the stone region in the sea urchin tooth prevented fabrication of larger samples to confirm the hypothesis. Additional research is needed to gain further insight into the effect of testing small samples. In this regard, we refer the reader to the work by Odette and co-workers, who pioneered a number of experiments and analysis approaches to deal with the identification of material constitutive behavior from the testing of small samples.[31,32]

In Situ SEM Wear Tests

The deformation behavior of the sea urchin tooth (i.e., self-sharpening) was examined using a novel *in situ* SEM wear experiment. In the experiments, a tooth glued into a special holder was compressed against an ultra-nanocrystalline diamond (UNCD) substrate (Figure 3A). Such experimental design is in direct contrast to conventional scratch experiments, where the tip is typically made from diamond and the wearing surface is the substrate.[33,34] Hence, our methodology focuses on revealing the role of tooth microstructure and constituent properties, on deformation and wearing, under well-controlled and measurable contact conditions. The diamond substrate is selected because of its hardness and wear resistance to activate and accelerate the tooth-chipping process. Details regarding the experimental setup and instrumentation employed in the wear experiments are provided in Experimental Procedures. In the experiments, a trapezoidal load-time profile is applied to the tooth to achieve a target compressive load, which is held constant during sliding. To mimic the motion of teeth inside the sea urchin mouthparts, scratching is performed along the radial direction (i.e., *y* direction in Figure 3A), where the opening and closing of teeth occur simultaneously.[20] Motion in this direction along with lateral motion of Aristotle's lantern, including rotation, shifting, and tilting, provide the required tooth functionalities of scraping, grinding, and biting.[14]

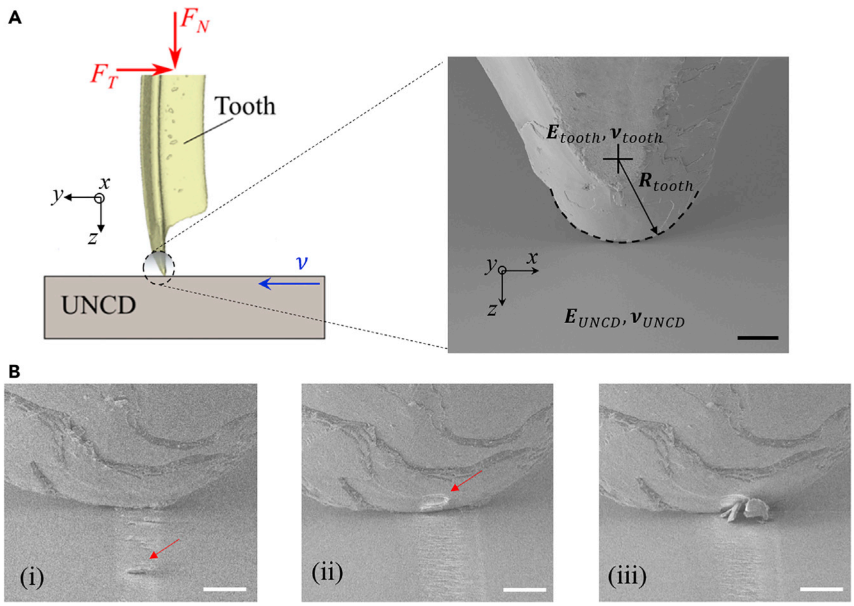

Figure 3. Components of the *In Situ* SEM Wear Experiment with the Tooth Tip in Contact with the Diamond Substrate

(A) Left panel: schematic of the tooth-UNCD substrate. F_N indicates the applied normal load on the tooth and V is the scratch velocity. Right panel: SEM image of the tooth in contact with the substrate. E_{Tooth}, ν_{Tooth} and E_{UNCD}, ν_{UNCD} are the elastic modulus and Poisson's ratio for the tooth and UNCD, respectively. R_{Tooth} is the tooth radius of curvature. Scale bar, 100 μm.

(B) Snapshots of recorded video during the wear experiment inside the SEM chamber. Scale bars, 30 μm. (i) The arrow indicates detached debris from the stone region. (ii) Onset of plate fracture. (iii) Chipping of plates from the convex side of the tooth.

To estimate the applied mean contact stress and the required load to reach such pressure on the tooth, we employed a Hertzian contact mechanics analysis. The analysis can be conceptualized as the plane-strain problem of a curved elastic body pressed against a rigid half-space. In this regard, the shape of the tooth is treated as a curve with an equivalent radius of curvature, R_{Tooth}, while the UNCD is considered as a rigid bulk half-space (see Figure 3A). Under these conditions, the force required to initiate tooth yielding is given by[35]

$$(F_N)_Y = \left(\frac{R_{Tooth}}{E^*}\right)^2 \cdot \frac{(\pi\sigma_Y)^3}{6}, \qquad \text{(Equation 1)}$$

where E^* is the reduced elastic modulus and σ_Y is the tooth yielding stress. The derivation of Equation 1 is given in Note S1. To ensure applicability of Equation 1, we performed several indentation experiments, on the UNCD substrate, at various maximum prescribed displacements. The load-displacement curves as well as the characterization of the tooth tip before and after the tests are provided in Figure S5. When the contact stress exceeds the stone yield stress, several "pop-in" events were observed in the load-displacement curves. SEM images of the tooth revealed deformation and cracking of the stone region. Thus, it was concluded that Equation 1 is a good estimator of the normal load needed to initiate yielding in the stone. We note that the biting forces from Aristotle's lanterns, from other species in Echinoidea, can range from ~1 to 50 Newton,[36] depending on the food source. The applied normal force in our experiment, for one tooth, ranges from hundreds of microNewtons up to 1 Newton, which results in 1- to ~5-Newton force for the whole lantern, due to the presence of five teeth.

The wear tests were carried out inside a scanning electron microscope using a commercial nanomechanical testing system (Alemnis). The details of sample preparation and implementation are given in Experimental Procedures. Wear tests were performed by translating the substrate in the y direction, as schematically illustrated in Figure 3A. The scratch parameters such as the tooth-tip velocity, V, as well as the sliding length, L, were chosen to perform the test in the stable friction regime.[37] The applied normal stress was selected to achieve a mean pressure equivalent to the yield stress of the tooth. This ensured that no cracks would appear during the initial loading step, as revealed by the quasi-static tooth indentation tests, while sliding could potentially cause tooth chipping upon accumulation of plasticity and damage. As shown in Figure 3B(i), some debris left by wear of the stone region is observed. As the stone region is worn and flattened, interface cracking between plates could initiate and propagate due to compression-shear loading and stress buildup in the calcite plates region. That this is indeed the case is observed in Figure 3B(ii) and (iii), where the SEM images reveal the shedding of primary plates on the convex side of the tooth. To the best of our knowledge, these are the first experimental images capturing plate chipping, in three dimensions, and the associated tooth self-sharpening mechanism.

To characterize the tooth-wearing phenomena and its relationship with independent variables, we conducted a dimensional analysis.[38] For this purpose the tooth wear, w, is expressed as a function of several dimensionless variables. We note that w may refer to the flattening of the stone and potential chipping of the plates. The former is calculated based on the change in contact area, while the latter is calculated from removed area, in the plate region, times the thickness of the plate. In both cases, w is characterized by comparing before and after SEM imaging in each wear test. In the case investigated here (i.e., when only the tooth wears), $w = f(\mu, F_N, V, t, H_{Tooth}, a)$. Here, F_N is the applied normal load, μ is the friction coefficient, V and t are the imposed sliding speed and duration, respectively, H_{Tooth} is the hardness of the tooth, and a is the contact radius. Using Buckingham's dimensional analysis,[39] the above equation can be reduced to a simpler nondimensional form given by (for details see Note S2)

$$\frac{w^i}{a^i} = f\left(\mu, \frac{L}{a}, \frac{F_N}{a^2 H_{Tooth}}\right). \qquad \text{(Equation 2)}$$

In the above equation, the power, "i" can be 2 for the flattening area ($w^2 \equiv A_{fl}$) or 3 for the volume of chipping ($w^3 \equiv V_{cp}$). In addition, F_N/a^2 can be defined as the nominal contact stress, and L is the sliding length equal to Vt. In the following, conditions under which self-sharpening may occur are revealed.

Two types of wear experiments were carried out. In one type, the load corresponding to the onset of yielding was kept constant during the entire sliding process (case W_{CL}). In a second type, the nominal contact stress was kept constant and equal to the stone yield stress (case W_{CS}). For the latter case, the flattened area was imaged and measured at specific sliding intervals of ~1,000 μm, and employed to update the contact area. Subsequently, an updated load was employed in order to keep F_N/a^2 constant. The force leading to a prescribed contact stress and the initial contact radius, a_0, were obtained from a contact mechanics analysis (see Note S1). Despite using the same initial contact stress in both cases (W_{CL} and W_{CS}), different wearing mechanisms were observed. Recorded SEM videos along with images of the tooth tips reveal, in both cases, flattening in the stone region. Videos of the wear experiments (Videos S1, S2, S3, and S4) are provided. When holding the load constant, W_{CL} case, and over the range of L/a_0 investigated, only an increase in flattened area, without plate chipping, was observed (Figure 4A). By contrast,

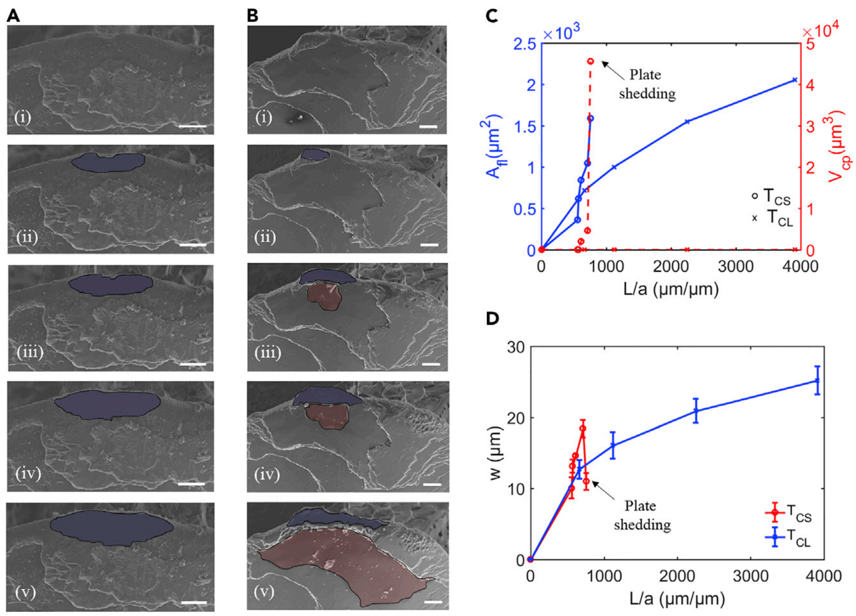

Figure 4. Characterization of Tooth Tips before and after Wear Tests

(A and B) SEM images of the tooth tip in pristine condition (i), and after wear tests (ii–v) as a function of scratch length: (A) under constant normal load, W_{CL}, and (B) under constant nominal contact stress, W_{CS}. The blue and red regions correspond to the flattened stone and chipped plates. Scale bars, 20 μm.

(C) Quantification of the stone flattened area (A_{fl}) and the chipped volume of the plates (V_{cp}) as a function of normalized scratch length, L/a_0.

(D) Width of the flattened region as a function of L/a_0. Error bars correspond to one standard deviation.

when the normal force was increased to maintain the nominal contact stress constant, W_{CS} case, continuous chipping and shedding of plates were observed (Figure 4B). This is also evident in a plot of measured flattened area and volume of chipped plates as a function of dimensionless sliding length, L/a_0 (see Figure 4C). This plot clearly shows that no plate chipping occurs for the W_{CL} case even when the dimensionless sliding distance is much larger than for the W_{CS} case. Careful examination of the stone flattening and chipped plates, shaded in red in Figure 4B, clearly reveals the self-sharpening mechanism. The stone flattened area increases up to a point because when a plate(s) is chipped, a part of the flattened area is simultaneously removed (Figure 4B(iii–v)). Microstructural features such as the connection between stone and plates seem to facilitate this process. Indeed, high-magnification SEM images (Figure S1) reveal that fibers in the stone region bend and penetrate the plate layering in the convex part of the tooth. Quantitatively, Figure 4C shows a jump in the chipping volume when a new plate(s) detach from the tooth tip. Interestingly, at the same L/a_0, a sharp reduction in the width of the flattened region is observed (Figure 4D), indicative of the self-sharpening process. These experimental results reveal that by keeping the normal load constant during the wear test, tip blunting occurs, whereas the tooth remains sharp when the nominal contact stress is kept constant and equal to the yield stress of the stone. These results were consistently observed in several experiments. Additional wear experimental results are given in Figure S6.

Nonlinear Finite-Element Simulations

To gain insight into the role of tooth microstructure, constituent properties, and their contribution to the self-sharpening mechanism, we conducted a nonlinear finite-element analysis of the wear process (Figure 5A). To this end, we used SEM

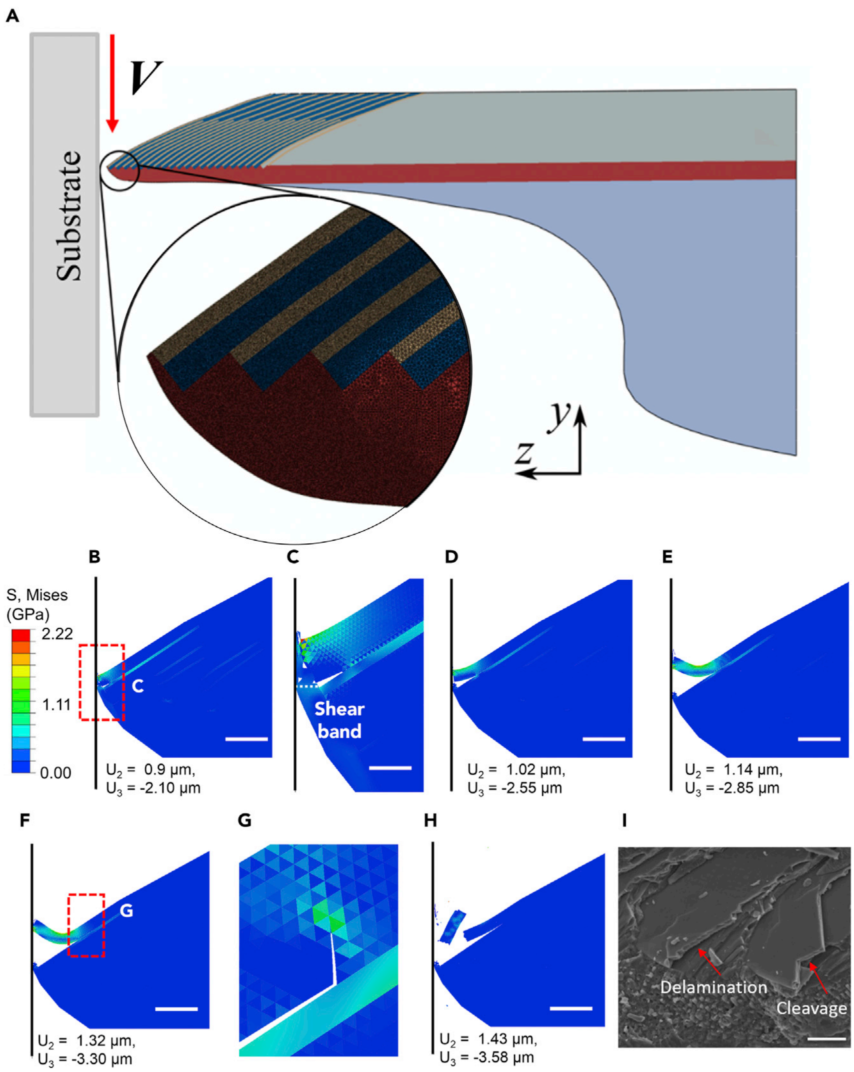

Figure 5. Finite-Element Analysis and Micromechanical Modeling of the Wear Process

(A) Tooth-substrate model.

(B–H) Contours of von Mises stress during the scratching process, in which flattening and detachment of the stone from the plate region is observed (B and C). U2 and U3 are simulated tip displacements along the *y* and *z* directions. (C) Zoom-in of the region shown in (B) depicting shearband formation in the stone. (D and E) Shear-off of a region of the stone and blunting leading to compression of outer plates. The chipping mechanism, consisting on plate delamination followed by cleavage, is shown in (F) to (H). (G) Zoom-in of the region shown in (F) where transition from delamination to cleavage takes place.

(I) SEM image of a sea urchin tooth displaying delamination as well as plate cleavage in the convex side of the tooth tip.

Scale bars, 10 µm (B, D, E, F, H, I) and 2 µm (C).

images of the longitudinal section of the tooth tip to build a two-dimensional model (see also Figure S7). The model consists of the stone, plates, keel, and interfaces between plates and stone. Dimensions and constitutive laws used in each region of the model are summarized in Experimental Procedures and detailed in Supplemental Information. A visco-plastic-damage model was used to describe the stone constitutive behavior and its fragmentation was modeled by element erosion. The keel region was simulated as a linear elastic material with effective homogenized properties. The plates, on the other hand, were implemented using an anisotropic elastic constitutive law and their cleavage (intra-plate fracture) was modeled via cohesive elements inserted between solid elements. The rationale behind this selection is based on the plate features (described in Tooth Architecture) and the observed fracture mechanisms. On the other hand, fracture between plates (inter-plate fracture) was modeled via interface elements possessing a strength, identified from micropillar tests, and cohesive energy obtained from literature reports. Details of the interface traction-separation law are provided in Note S3.

As shown in Figure 5A, a finite-element model of the tooth, with graded mesh size, was employed. The finest mesh (Figure 5A, inset), was placed in the region of the tip in contact with the substrate. A coarser mesh size was used toward the keel region. The simulation loading steps were the same as in the experiment, i.e., an approaching/compression step followed by a sliding step with velocity V, and a retraction step. In the approaching/compression step, the rigid substrate was displaced toward the tooth, in the ($-z$) direction, until a prescribed contact stress was achieved. In the sliding step, the tooth was displaced downward in the ($-y$) direction at a prescribed velocity V = 1 m/s. Finally, in the retraction step, unloading took place by moving the substrate in the z direction, until the tooth was out of contact with the substrate. The friction coefficient employed in the simulations, between the tooth and substrate, was experimentally measured during sliding tests and was found to have an average value of 0.4, which is in the same order as the friction coefficient measured during sliding of dolomite rocks[40] (Figure S6E).

Contour plots of von Mises stress, at the tip of the stone and plate regions, are shown in Figures 5B–5H. As the tooth is compressed, the stone undergoes large visco-plastic deformations, accumulates damage, and flattens (Figures 5B and 5C). Further compression triggers a shear band in the stone, where most of the plastic strain and damage accumulate, shearing off a part of the stone in direct contact with the substrate (Figure 5D). Such fragmentation of the stone is observed as stone debris in the experiments (Figure 3B(i)). The compression also results in inter-plate delamination, as the interface elements are subjected to mixed loading leading to decohesion. Indeed, as the contact region evolves, contact stresses build up, triggering crack initiation and propagation at interfaces (Figures 5B–5E). The loss of cohesion between plates enhances a bending mode that detaches the outer plate(s). Scratching exacerbates interface failure, which in turn results in plate removal when the plate(s) undergoes cleavage (where cracks deflect from the interface and penetrate into the plate, Figure 5G). As the process continues, chunks of the plate region chip away and detach from the tip (Figure 5H). Interestingly, the simulation predicts chipping in both the stone and plate regions, with the plate chip of variable size, a feature observed in the experiments (Figures 3B and 5I). We also note that depending on the interface and plate toughness, a competition between crack propagation by interface delamination and plate cleavage ensues. This is consistent with the argument that the organic layers surrounding the plates, at interfaces, promote and guide crack propagation.[14] Furthermore, the experimentally observed and modeled chip-formation mechanism shows that by tailoring the ratio between interface and crystal toughness, the size of the chip can be altered. In the sea urchin tooth, a range of chip sizes between 20 and 100 μm were imaged as the chipping process progressed (Figure 4B).

Conclusions

By creating a novel *in situ* SEM wear experiment, the self-sharpening mechanism previously hypothesized, for the sea urchin tooth, was visualized in three dimensions and associated contact conditions quantified. In particular, the synergy between tooth architecture, constituent mechanical properties, and wear mechanism were related to the tooth function. Furthermore, load conditions under which the self-sharpening mechanism is activated were identified. More specifically, we found that a threshold nominal contact stress of approximately the yield stress of the stone region is needed to activate the chipping mechanism. Plate chipping results from crack nucleation and propagation along interfaces between plates. The chip size is controlled by crack deflection into the plate when cleavage becomes energetically more favorable than continuous inter-plate delamination. Both experiments and simulations clearly reveal a transition from plate delamination to cleavage (see Figures 3 and 5), with the cleavage location defining the dimension of the chipping plate. Moreover, chip fracturing is also observed due to the three-dimensional nature of the deformation and stress state. Examination of the tip of tens of sea urchin teeth revealed features consistent with this chipping failure mode (Figure 5I). Moreover, the experimental force required to induce plate chipping is consistent with the biting forces estimated for the Aristotle lantern.[36] Hence, we conclude that the experiments and simulations reported here are representative of the sea urchin self-sharpening process involving stone wear followed by plate detachment and chipping. Another key feature revealed by this work, which was somewhat overlooked in prior work, is the role played by the stone quasi-brittle constitutive behavior. In fact, the material exhibits a combination of hardness, visco-plasticity, and damage that limits the contact stress and leads to wear, in the form of microscale debris. Formation of such debris takes place under specific conditions of combined normal and shear stresses. Note that in the absence of stone visco-plastic deformation and wearing, local stresses in the plate region, near the contact zone, would not reach the threshold required for plate delamination and chip formation. Interestingly, evolution achieved such functionality (modulation of tooth wear) by means of a fiber-matrix composite.

By performing nanomechanics experiments, the properties of the sea urchin tooth constituents were identified. When these were combined with nonlinear constitutive laws, a nonlinear finite-element model was successfully formulated to reveal local conditions of deformation and stress states leading to stone chipping, interface crack initiation and propagation, and ultimately plate chip formation leading to tooth self-sharpening. Interestingly, the simulations reported here not only captured the tooth-chipping phenomenon but also demonstrated the predictive capabilities of advanced nonlinear finite-element analyses based on independently parametrized material constitutive models. Therefore, the experimental-computational methodology established in this work can be broadly applied to other animals' teeth to elucidate microstructure-constituent property relationships on wearing mechanisms and overall functionality. This could also assist researchers in the dental industry to design new artificial teeth for humans with superior properties.

In closing, we note that model predictions of deformation and failure were consistent with the experimental measurements, which provides confidence in using nonlinear finite-element analysis to explore other potential combinations of microstructures, materials, and interface chemistries, beyond those encountered in natural materials. As such, this work paves the way for exploration of novel designs with application to the cutting and boring industries in which blade-cutting efficiency and wear resistance are highly sought after.

EXPERIMENTAL PROCEDURES

Teeth Extraction

Fifteen pink sea urchins (*Strongylocentrotus fragilis*) were collected in 2015 from an ocean depth of 340 m and then frozen. They were thawed at room temperature for sample preparation purposes. Their Aristotle's lanterns were extracted by cutting the connective tissue around the perimeter of the lantern and rinsing in distilled water. Teeth were carefully slid out from the lantern using forceps. They were then rinsed again in distilled water and dried out at room temperature for different characterization purposes and wear experiments.

Indentation Maps

Teeth were mounted in the longitudinal and transverse directions using EpoThin2 resin. The samples were polished progressively using SiC papers down to P2500 followed by diamond polishing with a paste suspension of 3 μm and 1 μm. A final polishing step with alumina suspension down to 50 nm was employed. The roughness of the samples, measured with an optical profilometer, had a root-mean-square (RMS) of ~27 nm. Nanoindentation measurements were performed with an MTS indenter XP equipped with a continuous stiffness measurement (CSM) indenter head. Indentations were made with a Berkovich tip to an indentation depth of 300 nm (which is around ten times the roughness of the sample) and a holding time of 60 s. The thermal drift was set to 0.1 nm/s. In the CSM mode, a 2-nm oscillation with a frequency of 45 Hz was prescribed in the measurement. Indentation maps with spacing of 10 μm between each indent were obtained. For each indentation point, modulus and hardness were averaged between 100- and 300-nm indentation depths. The optical images of the samples along with indentation maps for both longitudinal and transversal directions are provided in Figure S2.

Cyclic Indentation Experiments

Three tests over different regions of the stone were performed. Parameters used in the tests were holding time 150 s, maximum load 180 mN, and constant loading and unloading rates of 0.45 mN/s. Several cycles were performed using a Berkovich tip. The thermal drift was set to 0.1 nm/s.

Micropillar Compression Tests

Samples were polished using the procedure described above. A 30-nm thick Pt film was sputtered to minimize drift during focused ion beam (FIB) milling. Micropillars were fabricated from the tooth samples using an annular FIB milling technique in an FEI Nova 600 NanoLab instrument. To this end we used a staged approach, which applied successively finer beam currents in the range of 6.5 to 1 nA, to produce well-polished specimens. All micropillars were cut at an acceleration voltage of 30 kV. Each micropillar was fabricated with a nominal diameter (5 μm and 10 μm) and a length-to-diameter ratio of 3:1. A minimum of three replication experiments were performed for each testing case. Micropillar compression testing was performed using an Alemnis micromechanical testing platform under *in situ* electron imaging in an FEI Nova 600 instrument. Uniaxial compression tests were performed using displacement control at a nominal strain rate of $\sim 8 \times 10^{-4}$/s with a 10-μm flat-tip diamond indenter. Applied forces were measured with an in-line load cell having a nominal RMS noise of 4 μN. The applied strains were determined after correction for thermal drift, machine compliance, tapering of micropillars, and sink-in effects of the micropillar into the supporting tooth. The shear strain was calculated using the strain transformation relationship: $\gamma = 2(\varepsilon_N - \nu\varepsilon_N)\sin(\theta)\cos(\theta)$, where ε_N and ν are the normal compression strain and Poisson's ratio, respectively, and θ is the orientation angle of the inclined surface, which was equal to 30°.

Tooth-Tip Compression against a Diamond Substrate

To evaluate the tooth-tip condition at the beginning of wear experiments, we performed tooth-tip compression experiments for several tip contact stresses. To this end, we calculated the maximum load for each contact stress, from $0.5\sigma_Y$ to $2\sigma_Y$, based on contact mechanics analysis. The experiments were conducted under load control with a loading time of 20 s. The characterization of the tip before and after each experiment was performed using a scanning electron microscope. The prepared tooth and its tip characterization are shown in Figures S5A–S5E. Other than a slight flattening, no obvious damage was observed at the tooth tip for contact stresses smaller than the stone yield stress. However, for stresses above the stone yield stress, cracks appeared at the tooth tip as shown in Figures S5D and S5E. These observations could be correlated to features in the load-displacement curves. Curves for a constant stress equal to the stone yield stress and higher are reported in Figures S5F and S5G. Interestingly, the curves for contact stress above the yielding point contain multiple "pop-ins" and "pop-outs" indicative of damage and fracture occurring at the tip of the tooth.

Wear Experiments

To understand the wearing and chipping phenomena, we conducted *in situ* SEM wear tests using an Alemnis nanomechanical tester.[41] Friction coefficient measurements were performed with an MTS nanoindenter XP instrument. The specimens for the wear experiments were prepared as follows. Since sea urchins' teeth are long and have a curvy shape, first they were cut into a 4-mm length for mounting purposes. A customized holder was designed and manufactured that could fit into both the MTS nanoindenter XP machine and the Alemnis tester. Pristine teeth were selected and mounted into the holder using epoxy adhesive (Loctite 1C Hysol Epoxi-patch). They were then coated with 8 nm of osmium. SEM images of the tooth tips were taken before the scratch experiments. UNCD (1 μm thick) deposited by chemical vapor deposition on a silicon wafer[42] was used as the substrate in the wear experiments. The substrate was glued with epoxy adhesive on an aluminum stub and fitted into a holder of the instrument. For *in situ* SEM scratch tests, the Alemnis tester was installed inside a Nova NanoSEM 600 operating at 10 kV and 2.6 nA. The tooth holder was fitted into a gantry containing a piezo actuator and a displacement sensor, which is used to prescribe the displacement. The substrate holder was fitted into the load sensor. As the tooth came in contact with the UNCD substrate, the load was measured by the sensor.[41] Before initiation of sliding, the tooth was compressed to a maximum prescribed load over 20 s loading time with a 10 s holding time. The wear experiments were then carried out at a constant sliding speed of 10 μm/s and a constant load. Videos were recorded to capture the process of wearing and chipping. Relative motion between tooth and substrate was obtained by moving the substrate at the prescribed speed. After a sliding distance of 1,000 μm, teeth were removed, imaged, and characterized. In all accelerated wear experiments, the initial contact stress was set to the yielding stress of the stone. Characterization of the tooth tips for the constant load and constant contact stress cases are provided in Figures S6A–S6D. For the purpose of friction coefficient measurements, the same teeth were used as tips in the MTS nanoindenter setup, which possesses both normal and lateral force measurements. The friction coefficient for three teeth at two different normal loads was measured (Figure S6E).

Nonlinear Finite-Element Analysis

The commercial finite-element code ABAQUS/Explicit 6.16 was used to perform numerical analyses. Two different analyses were carried out: the first was for the stone cyclic indentation experiments, which were used to identify parameters for a visco-plastic model with damage[25] (see Supplemental Information for details); the second was analysis of the wear experiment. The indentation analysis consisted of an axisymmetric (rigid) 140.6° conical diamond indenter compressing against a tooth stone substrate 30 μm in width and 40 μm in depth. The two-dimensional axisymmetric mesh was constructed to be fine near the indentation surface (the element type is CAX3 axisymmetric elements with minimum size of 0.25 μm) and coarser toward the base (Figure S8A). The simulation included three stages: loading, holding, and unloading, as in the experiments. During loading, a rigid surface modeling the indenter tip moved downward and penetrated the specimen up to a maximum prescribed load. During unloading, the indenter tip retracted to the initial position. Contour plots of von Mises stress and equivalent plastic strain showed localization of deformation under the indenter tip and at the edge of the contact. Through an iterative procedure (described in Supplemental Information), the stone model parameters, reproducing the experimental load-displacement cyclic curves, were identified (Figure S8B). The complete set of parameters is listed in Table S1. The extracted load-displacement history, from the FE model, is compared with the experimental data in Figure 2A. The calculated modulus from the unloading data exhibits a decreasing trend, as a function of indentation depth, which was related to damage accumulation consistent with observed cracking around the fibers (Figures 2B and 2C). In the wear analysis, the plates were modeled as anisotropic elastic bodies with moduli corresponding to the calcite single crystal, which possesses a trigonal-rhombohedral structure[43] (Table S2). It was previously shown that the *c* axis of the crystal is tangential to the tooth surface curvature.[23] This feature was implemented, at each quadrature point of the mesh in the plates, by tensorial definition of the elastic constitutive law along the direction of the crystal lattice. To model fracture, we embedded cohesive elements between and within plates to capture both interface crack initiation and propagation between plates and calcite single-crystal cleavage. These elements have zero thickness with a triangular traction-separation law, although their properties are different (Figure S8H). To accommodate mode coupling, we define an effective fracture energy at failure (Table S3). In addition to employing an explicit contact algorithm between the stone and plates, the self-contact algorithm, based on the penalty method, was used. The keel part was modeled as an isotropic body with linear elastic property (Table S4). The mass densities of the stone, plates, and keel were considered the same and equal to 2.7 g/cm^3, while the mass density of interfaces is considered similar to the organic sheath layer, ~0.5 g/cm^3. For the base materials (stones, plates, and so forth), 3-node (triangular) plane-strain elements CPE3 were used. For interfaces (between components and within components), 4-node (quadrilateral) cohesive elements COH2D4 were used. The largest element has a dimension of 12 μm, and the mesh is refined at the contact area with the smallest element having a characteristic dimension of ~0.25 μm.

SUPPLEMENTAL INFORMATION

Supplemental Information can be found online at https://doi.org/10.1016/j.matt.2019.08.015.

ACKNOWLEDGMENTS

The authors gratefully acknowledge financial support from a Multi-University Research Initiative through the Air Force Office of Scientific Research (AFOSR-FA9550-15-1-0009). We also thank the Scripps Institution of Oceanography of San Diego for providing the tooth specimens. The authors also acknowledge support from the Center for Nanoscale Materials (Argonne National Lab). A.Z. thanks Zhaowen Lin for conducting one of the pillar tests.

AUTHOR CONTRIBUTIONS

The design of the study was devised by H.D.E., J.M., M.F., and A.Z. The SEM imaging, nanoindentation, dimensional analysis, and *in situ* wear tests were performed by A.Z. Micropillar compression tests were conducted by M.D. Finite-element simulations were carried out by D.R. and H.N. The manuscript was written by H.D.E. and A.Z. with contributions from all of the authors.

DECLARATION OF INTERESTS

The authors declare no competing interests.

Received: April 27, 2019
Revised: June 27, 2019
Accepted: August 14, 2019
Published: September 18, 2019

REFERENCES

1. Strait, S.G. (1997). Tooth use and the physical properties of food. Evol. Anthropol. *5*, 199–211.

2. Ungar, P.S. (2014). Teeth: A Very Short Introduction (OUP Oxford).

3. Zok, F.W., and Miserez, A. (2007). Property maps for abrasion resistance of materials. Acta Mater. *55*, 6365–6371.

4. Amini, S., and Miserez, A. (2013). Wear and abrasion resistance selection maps of biological materials. Acta Biomater. *9*, 7895–7907.

5. Irish, J.D., and Scott, G.R. (2015). A Companion to Dental Anthropology (John Wiley & Sons).

6. Imbeni, V., Kruzic, J.J., Marshall, G.W., Marshall, S.J., and Ritchie, R.O. (2005). The dentin-enamel junction and the fracture of human teeth. Nat. Mater. *4*, 229–232.

7. Chai, H., Lee, J.J.W., Constantino, P.J., Lucas, P.W., and Lawn, B.R. (2009). Remarkable resilience of teeth. Proc. Natl. Acad. Sci. U S A *106*, 7289–7293.

8. Ungar, P.S. (2015). Mammalian dental function and wear: a review. Biosurf. Biotribol. *1*, 25–41.

9. Huang, M., Wang, R., Thompson, V., Rekow, D., and Soboyejo, W. (2007). Bioinspired design of dental multilayers. J. Mater. Sci. Mater. Med. *18*, 57–64.

10. Niu, X., Rahbar, N., Farias, S., and Soboyejo, W. (2009). Bio-inspired design of dental multilayers: experiments and model. J. Mech. Behav. Biomed. *2*, 596–602.

11. Ma, Y., Weiner, S., and Addadi, L. (2007). Mineral deposition and crystal growth in the continuously forming teeth of sea urchins. Adv. Funct. Mater. *17*, 2693–2700.

12. Shaw, J.A., Macey, D.J., and Brooker, L.R. (2008). Radula synthesis by three species of iron mineralizing molluscs: production rate and elemental demand. J. Mar. Biol. Assoc. U.K. *88*, 597–601.

13. Wang, R.Z., Addadi, L., and Weiner, S. (1997). Design strategies of sea urchin teeth: structure, composition and micromechanical relations to function. Philos. Trans. R. Soc. Lond. B Biol. Sci. *352*, 469–480.

14. Killian, C.E., Metzler, R.A., Gong, Y.T., Churchill, T.H., Olson, I.C., Trubetskoy, V., Christensen, M.B., Fournelle, J.H., De Carlo, F., Cohen, S., et al. (2011). Self-sharpening mechanism of the sea urchin tooth. Adv. Funct. Mater. *21*, 682–690.

15. Frank, M.B., Naleway, S.E., Wirth, T.S., Jung, J.Y., Cheung, C.L., Loera, F.B., Medina, S., Sato, K.N., Taylor, J.R.A., and McKittrick, J. (2016). A protocol for bioinspired design: a ground sampler based on sea urchin jaws. J. Vis. Exp. https://doi.org/10.3791/53554.

16. Stock, S.R. (2014). Sea urchins have teeth? A review of their microstructure, biomineralization, development and mechanical properties. Connect. Tissue Res. *55*, 41–51.

17. Robach, J.S., Stock, S.R., and Veis, A. (2006). Mapping of magnesium and of different protein fragments in sea urchin teeth via secondary ion mass spectroscopy. J. Struct. Biol. *155*, 87–95.

18. Lawrence, J.M. (2013). Sea Urchins: Biology and Ecology, *Vol. 38*, Third Edition (Academic Press).

19. Ziegler, A., Schroder, L., Ogurreck, M., Faber, C., and Stach, T. (2012). Evolution of a novel muscle design in sea urchins (Echinodermata: Echinoidea). PLoS One *7*, e37520.

20. Carnevali, M.C., Wilkie, I., Lucca, E., Andrietti, F., and Melone, G. (1993). The Aristotle's lantern of the sea-urchin *Stylocidaris affinis* (Echinoida, Cidaridae): functional morphology of the musculo-skeletal system. Zoomorphology *113*, 173–189.

21. Ma, Y., Cohen, S.R., Addadi, L., and Weiner, S. (2008). Sea urchin tooth design: an "All-Calcite" polycrystalline reinforced fiber composite for grinding rocks. Adv. Mater. *20*, 1555.

22. Ma, Y.R., Aichmayer, B., Paris, O., Fratzl, P., Meibom, A., Metzler, R.A., Politi, Y., Addadi, L., Gilbert, P.U.P.A., and Weiner, S. (2009). The grinding tip of the sea urchin tooth exhibits exquisite control over calcite crystal orientation and Mg distribution. Proc. Natl. Acad. Sci. U S A *106*, 6048–6053.

23. Goetz, A.J., Griesshaber, E., Abel, R., Fehr, T., Ruthensteiner, B., and Schmahl, W.W. (2014). Tailored order: the mesocrystalline nature of sea urchin teeth. Acta Biomater. *10*, 3885–3898.

24. Oliver, W.C., and Pharr, G.M. (1992). An improved technique for determining hardness and elastic-modulus using load and displacement sensing indentation experiments. J. Mater. Res. *7*, 1564–1583.

25. Zhang, J.Z., Michalenko, M.M., Kuhl, E., and Ovaert, T.C. (2010). Characterization of indentation response and stiffness reduction of bone using a continuum damage model. J. Mech. Behav. Biomed. *3*, 189–202.

26. Lucchini, R., Carnelli, D., Ponzoni, M., Bertarelli, E., Gastaldi, D., and Vena, P. (2011). Role of damage mechanics in nanoindentation of lamellar bone at multiple sizes: experiments and numerical modeling. J. Mech. Behav. Biomed. *4*, 1852–1863.

27. Wang, R.Z. (1998). Fracture toughness and interfacial design of a biological fiber-matrix ceramic composite in sea urchin teeth. J. Am. Ceram. Soc. *81*, 1037–1040.

28. Schwiedrzik, J., Raghavan, R., Burki, A., LeNader, V., Wolfram, U., Michler, J., and Zysset, P. (2014). In situ micropillar compression reveals superior strength and ductility but an absence of damage in lamellar bone. Nat. Mater. *13*, 740–747.

29. Yilmaz, E.D., Jelitto, H., and Schneider, G.A. (2015). Uniaxial compressive behavior of micro-pillars of dental enamel characterized in multiple directions. Acta Biomater. *16*, 187–195.

30. Yilmaz, E.D., and Schneider, G.A. (2016). Mechanical behavior of enamel rods under micro-compression. J. Mech. Behav. Biomed. *63*, 183–194.

31. Krumwiede, D.L., Yamamoto, T., Saleh, T.A., Maloy, S.A., Odette, G.R., and Hosemann, P. (2018). Direct comparison of nanoindentation and tensile test results on reactor-irradiated materials. J. Nucl. Mater. *504*, 135–143.

32. Odette, G.R., He, M., Gragg, D., Klingensmith, D., and Lucas, G.E. (2002). Some recent innovations in small specimen testing. J. Nucl. Mater. *307-311 Pt 2*, 1643–1648.

33. Schoberl, T., and Jager, I.L. (2006). Wet or dry—hardness, stiffness and wear resistance of biological materials on the micron scale. Adv. Eng. Mater. *8*, 1164–1169.

34. Pontin, M.G., Moses, D.N., Waite, J.H., and Zok, F.W. (2007). A nonmineralized approach to abrasion-resistant biomaterials. Proc. Natl. Acad. Sci. U S A *104*, 13559–13564.

35. K.L. Johnson, Contact mechanics, Cambridge University Press, 1987.

36. Ellers, O., and Telford, M. (1991). Forces generated by the jaws of clypeasteroids (Echinodermata: Echinoidea). J. Exp. Biol. *155*, 585–603.

37. Ruina, A. (1983). Slip instability and state variable friction laws. J. Geophys. Res. *88*, 359–370.

38. Williams, J.A. (2005). Wear and wear particles—some fundamentals. Tribol. Int. *38*, 863–870.

39. Buckingham, E. (1914). On physically similar systems, illustrations of the use of dimensional equations. Phys. Rev. *4*, 345–376.

40. Ohnaka, M. (1975). Frictional characteristics of typical rocks. J. Phys. Earth *23*, 87–112.

41. Rabe, R., Breguet, J.M., Schwaller, P., Stauss, S., Haug, F.J., Patscheider, J., and Michler, J. (2004). Observation of fracture and plastic deformation during indentation and scratching inside the scanning electron microscope. Thin Solid Films *469*, 206–213.

42. Espinosa, H.D., Peng, B., Prorok, B.C., Moldovan, N., Auciello, O., Carlisle, J.A., Gruen, D.M., and Mancini, D.C. (2003). Fracture strength of ultrananocrystalline diamond thin films—identification of Weibull parameters. J. Appl. Phys. *94*, 6076–6084.

43. Chen, C.C., Lin, C.C., Liu, L.G., Sinogeikin, S.V., and Bass, J.D. (2001). Elasticity of single-crystal calcite and rhodochrosite by Brillouin spectroscopy. Am. Mineral. *86*, 1525–1529.